Available online at www.sciencedirect.com

ScienceDirect

Ceramics International 41 (2015) 43–52

CERAMICS INTERNATIONAL

www.elsevier.com/locate/ceramint

Preparation of monodisperse silica spheres and determination of their densification behaviour

Berna Topuz*, Deniz Şimşek, Muhsin Çiftçioğlu

Chemical Engineering Department, İzmir Institute of Technology, Urla, İzmir, Turkey

Received 6 May 2014; received in revised form 13 July 2014; accepted 22 July 2014
Available online 4 August 2014

Abstract

Monodisperse silica spheres in the 50–520 nm size range were prepared by using the Stober process. Diffusive growth has been determined from Nielsen chronomal analysis for the 520 and 310 nm monodisperse silica spheres. The densification behaviour and evolution of the microstructure of the sphere compacts indicated an inverse dependence of shrinkage rate on the sphere size due to viscous sintering. The increase in sphere size from 50 to 500 nm shifted the densification temperature from ~1120 °C to 1240 °C. The amorphous nature of the spheres was conserved up to 1200 °C where cristobalite crystal nucleation started and complete transformation to cristobalite phase has been observed upon heat treatment at 1300 °C. The activation energies for viscous sintering according to the Frenkel and Mackenzie/Shuttleworth models were calculated as 125 and 335 kJ/mol, respectively. These substantially low activation energies can be attributed to the presence of a significant level of silanol groups.

Keywords: Stober process; Silica spheres; Growth mechanism; Densification

1. Introduction

The use of sol–gel derived monosize silica spheres in the 5–700 nm size range can make the nanodesign of porous materials for specific applications like membranes with interconnected pore structures, catalysts and photonic band gap crystals possible [1–4]. A predefined pore structure can be easily designed by varying the diameter and the packing behaviour of monodisperse silica spheres. There are several approaches for preparing colloidal spheres with narrow particle size distributions [5]. The colloidal sol–gel process, which was originally developed by Stober and coworkers in 1968, is the most commonly used method for the preparation of monodisperse silica sols [6]. In the so called Stober process monodisperse silica spheres with sizes in the 5–2000 nm range can be synthesised by the ammonia-catalysed hydrolysis and condensation of silicon alkoxides in solvents containing the necessary water for these reactions. The monodisperse silica sphere size depends upon the water and ammonia contents, the solvent type and the synthesis temperature [7–10].

The size of the silica spheres prepared by the Stober process is mainly controlled by the relative rates of nucleation and growth. These two events should occur separately in order to prepare monodispersed uniform particles along with a slow growth rate according to the LaMer model [11]. The growth of spherical particles depends upon the interfacial free energy between a growing nucleus and its chemical environment. The supersaturation necessary for the formation of spheres is provided by the hydrolysis and condensation reactions. As the reactions proceed, the intermediate $[Si(OC_2H_5)_{4-x}(OH)_x]$ concentration increases rapidly generating a supersaturated solution and eventually at a critical level of supersaturation the spheres begin to nucleate. The growth of these nuclei decreases the concentration, after which nucleation terminates. The spheres continue to grow by molecular addition until all intermediates are consumed [11]. The controlled parameters including, type of reactants, reaction temperature,

*Corresponding author. Present address: Chemical Engineering Department, Ankara University, 06100 Tandogan, Ankara, Turkey.
Tel.: +90 532 5137502.
E-mail address: bernatopuz@gmail.com (B. Topuz).

http://dx.doi.org/10.1016/j.ceramint.2014.07.112
0272-8842/

NH_3/alkoxide and H_2O/alkoxide molar ratios, as well as the solvent type influence the formation of the nuclei and the subsequent growth process.

In the last couple of decades extensive work have been conducted for the development of a better understanding on the formation and growth mechanisms of the monodisperse silica spheres by using different techniques including Si NMR, photon correlation spectroscopy, small angle X-ray scattering, and dynamic light scattering [8,9,12–14]. Monomer addition and controlled addition models have been proposed to explain the monodispersivity of the spherical silica particles. Based on the monomer addition model, the total number of nuclei is fixed (LaMer like burst) initially, and then the resultant sphere size is determined by the growth process which can be controlled by the total concentration of the alkoxide precursor. Nucleation is controlled by the condensation reactions between the reactive monomers. The narrow sphere size distributions are preserved during the growth due to the addition mechanism. The second approach for providing monodispersity is the aggregative growth model where a broad size distribution of primary spheres is assumed to be present in the beginning of the growth process. While nucleation happens continuously, progress of the reaction occurs by the preferential growth of bigger spheres at the expense of smaller spheres providing a narrow sphere size distribution. The rate-determining step is the formation of primary spheres. This model is based on colloidal stability which in turn depends largely to the surface charge of the particles [7]. van Blaaderen et al. [8] claimed that both mechanisms are additive for the formation of spheres in which nucleation is controlled by the aggregation of soluble species while the monomer addition leads to the smoothing of the surface by condensation. The rate-determining step has been found to be the formation of the hydrolysed monomer by ^{13}C NMR [8].

The growth and structural development of spheres occur through either diffusion-limited or reaction-limited processes. The major steps for growth can be stated as the transport of mass to the interface (diffusion) and the incorporation into the particle by surface condensation reactions. The relative rates of these kinetic processes determine the packing characteristics of the final structure, whether it is extended with low fractal dimensions heavily or more compact/dense.

The use of monodisperse silica spheres for the theoretical interpretations of sintering models has been also the subject of considerable body of work [15–17]. Sintering might be accomplished by different mechanisms, including viscous flow, surface/lattice/grain boundary diffusion, and vapour transport depending upon the materials sintered and sintering conditions. Viscous flow is the dominating transport mechanism for amorphous material sintering while the crystalline materials sinter by solid-state diffusion. Analysis of the dominant sintering mechanism is one of the challenges due to the relatively complicated nature of the microstructural evolution in the course of sintering depending on the initial powder properties/microstructure.

In this study, the growth of the silica spheres was investigated by using dynamic particle size data and chronomal analysis was applied in order to understand the growth mechanism. Dilatometric analysis was used to establish a better understanding of the relationships between the particle size and the densification behaviour of monodisperse silica sphere compacts.

2. Material and methods

Monodisperse silica spheres in the 50–520 nm range were prepared by the Stober process [6]. NH_4OH (28–30 wt% NH_3, Aldrich)–ethyl alcohol (99.8%, Riedel) solution was added to the Tetraethylorthosilicate (TEOS 98%, Aldrich)–ethyl alcohol solution (0.28 M Si^{4+} equivalent) during the sphere synthesis. TEOS:NH_3:H_2O:EtOH molar ratio of 1:4.3:12.8:40.7 was used for the precipitation of 310 nm spheres respectively. Synthesis of the monodisperse silica spheres was completed under constant stirring of the precipitation solution overnight at room temperature. The spheres were recovered by centrifugation, washed with ethanol and dried overnight at 40 °C. The molar ratios of the constituents and the sizes of the spheres obtained are further tabulated in Table 1.

Monodisperse silica spheres dispersed in ethanol were centrifuged and dried at 40 °C to prepare the ordered sphere compacts. These binder free dried monodisperse silica sphere powders in the 50–520 nm range were consolidated into cylindrical compacts (5 mm in diameter and 4 mm in thickness) by uniaxial pressing under a pressure of 180 MPa for dilatometric densification behaviour characterizations.

Dynamic light scattering (DLS) was used to determine the particle size distributions and the surface charges of the spheres (ZetaSizer 3000 HS, Malvern). The samples were diluted tenfold with ethanol in order to terminate the reactions before the DLS experiments. The nature of the packing and the monodispersivity/size of the spheres were examined by SEM (Philips XL30 SFEG) analysis of the fracture surfaces of the centrifuged/densified sphere compacts. TGA (LAB SYS Seteram) was used for the thermal behaviour determination of the spheres where the samples were heated at a rate of 3 °C/min up to 1300 °C in air. The densification behaviour of the spheres was investigated by determining the dilatometric shrinkage curves (Linseis, L76/150B) with a heating rate of 5 °C/min up to 1300 °C.

3. Results and discussion

The size and structure of the spheres depend upon the rates of hydrolysis and condensation reactions. The effect of sol–gel process parameters on the final sphere size in a relatively wide range (5–700 nm) was investigated in this work. Spheres with various sizes were prepared by varying the NH_3/TEOS,

Table 1
Synthesis parameters employed for the preparation of monodisperse spheres.

Size (nm)	TEOS concentration (M)	TEOS	NH_3	H_2O	EtOH
520	0.20	1	2.9	53.6	58.6
310	0.28	1	4.3	12.8	40.7
260	0.28	1	4.3	14	40.7
50	0.20	1	0.43	53.6	58.6

H_2O/TEOS molar ratios as well as the initial TEOS concentration [10]. As stated by the LaMer model [11], when all nuclei are formed during the same short nucleation period, silica spheres with narrow particle size distributions could be obtained as shown in Fig. 1 for 310 and 520 nm spheres. The mean sphere size was estimated from the SEM micrograph as 310 ± 8 nm which was also verified by the very sharp DLS based size distribution peak located at about 300 nm in Fig. 1a. The DLS particle size distribution of the 520 nm silica spheres along with the SEM micrograph is given in Fig. 1b, which again shows a high degree of monodispersity.

The variation of the sphere sizes with time for 310 nm and 520 nm spheres are given in Fig. 2. The sudden change in turbidity of the sol was observed in the early stages of the reaction after about 1 min and the mean sphere size was measured as about 100 nm after 2 min for 520 nm spheres. Almost constant sphere size of 500 nm was obtained within an hour and further a slight increase in sphere size with time most likely due to Ostwald ripening of the reduced primary spheres occurred afterwards. The growth of the 310 nm spheres was comparatively slower where the first size determination was conducted after 10 min. Depending on the degree of supersaturation, a power law of either 1/2 or 1/3 would be expected during the early stage of nucleation [18]. The variation of the sphere size with time indicated that growth regime is $t^{1/2}$ dependent which is indicative of diffusive type of growth after the initial 1–2 min as shown in Fig. 2 [13]. Diffusive type of growth has also been reported for the coarsening of ZnO and TiO_2 nanoparticles [19].

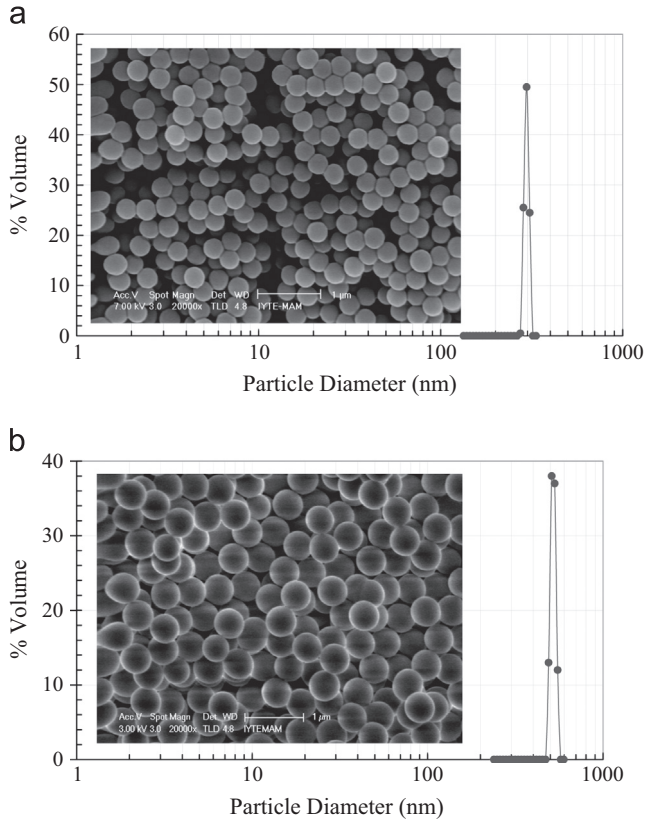

Fig. 1. Particle size distribution and SEM micrographs (20kX) of monodispersed spheres (a) 310 nm and (b) 520 nm.

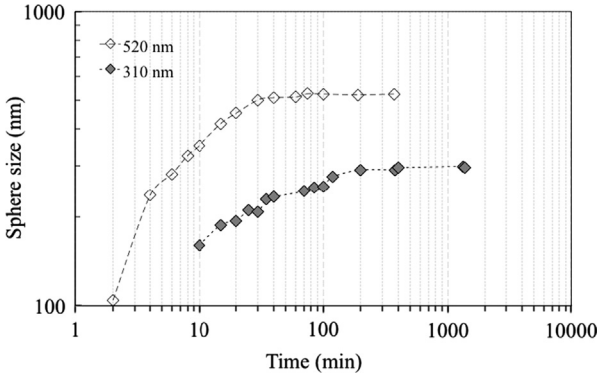

Fig. 2. The variation of sphere size with time for 310 and 520 nm spheres.

Nielsen's chronomal (dimensionless time parameter) analysis was also applied to elucidate the rate-limiting step during the growth of spheres by assuming constant particle density and narrow particle size distribution [20]. For diffusion-controlled growth regime, growth rate can be expressed as

$$\frac{dr}{dt} = \frac{vD(C-S)}{r} \tag{1}$$

where v is the molar volume (27.2 cm^3/mol; [21]), D is the diffusion coefficient (cm^2/s), C is the concentration and S is the solubility (116 ppm SiO_2 at 25 °C) [22]. The extent of reaction (α_d) with time can be defined as follows:

$$\alpha_d = \left(\frac{r(t)}{r_e}\right)^3 = \frac{C_o - C}{C_o - S} \tag{2}$$

where r_e is the equilibrium radius and C_o is the initial concentration. For diffusion-controlled growth, the α_d dependent chronomal function (I_d) is expressed as

$$I_d(\alpha_d) = \int_0^{\alpha_d} x^{1/3}(1-x)^{-1}dx \tag{3}$$

and Eqs. (1)–(3) combined leads a chronomal equation

$$t = K_d I_d \tag{4}$$

where K_d is a factor converting a chronomal to time and expressed as follows:

$$K_d = \frac{{r_e}^2}{3vD(C_o - S)} \tag{5}$$

The variation of the chronomal analysis derived concentration and extent of reaction with time for 310 and 520 nm spheres are given in Fig. 3a and b, respectively. The concentration decrease and α_d values increase much more rapidly for 520 nm spheres and accordingly the time for the termination of the reaction was much shorter than those for 310 nm spheres. This observed difference in α_d values most likely is due to the differences in the relative contributions of nucleation and growth processes for both sizes. Short reaction time for 520 nm could be due to the higher hydrolysis and condensation rates strongly affecting the total number of nuclei formed and their growth rates.

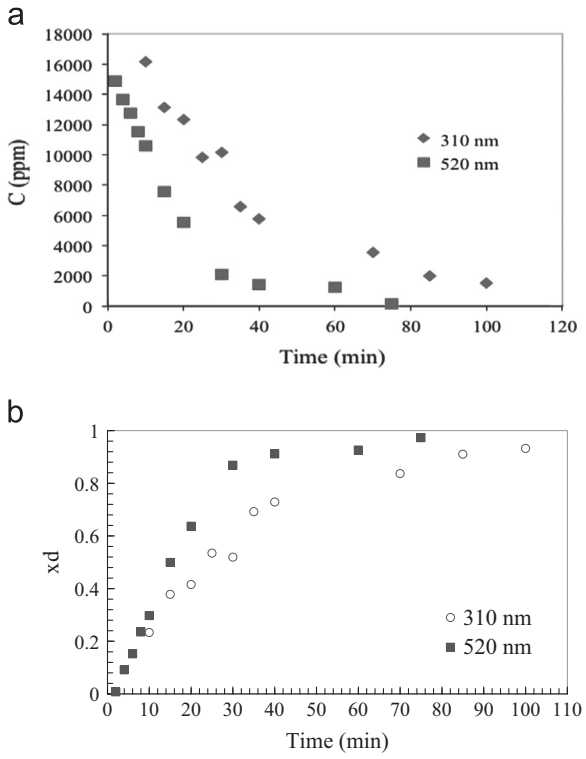

Fig. 3. The variation of the chronomal analysis based on (a) concentration and (b) extent of reaction with time for 310 and 520 nm spheres.

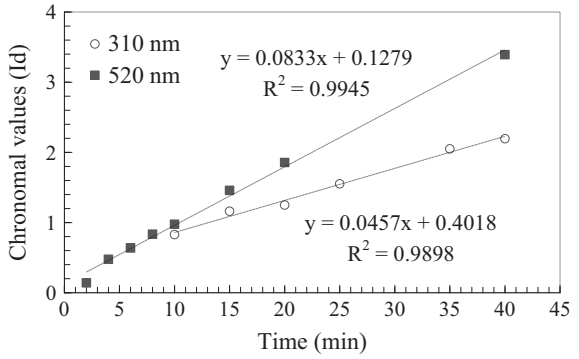

Fig. 4. Chronomal values with reaction time for diffusion limited growth of 310 and 520 nm spheres.

Chronomal values of the diffusion limited growth for 310 and 520 nm spheres with time are given in Fig. 4. The presence of a linear relation between reaction time and corresponding chronomal values ($R^2 > 0.95$) indicated that diffusion is the rate-limiting step for the growth of spheres. The chronomal analysis derived diffusion coefficients were determined as 2.5×10^{-10} cm^2/s and 3.1×10^{-11} cm^2/s for the 520 and 310 nm spheres respectively. Similar chronomal analysis was also conducted for reaction controlled growth regime. The regression analysis of the data has shown significantly lower coefficients (R^2-values) which was concluded to be an indication of the absence of reaction controlled growth.

SEM micrographs of the fracture surfaces of 310 nm ordered sphere compacts are shown in Fig. 5. Ordering is long range and spheres are closely packed in a hexagonal arrangement with some local defects (Fig. 5a). Ordered spheres in dried states reflected brilliant colours due to Bragg diffractions of visible light. The range of colours depends on the size of the spheres, which determines the lattice parameter and the refraction at the surface. It is well known that in any opal displaying colours, the spheres are uniform in size and they may pack regularly and regions over which the colour is the same have the same orientation. However, light scattering from voids induced by irregular packing leads to milky colour [23]. The ordered structure develops when the repulsive barrier is sufficient to allow the particles to arrange into dense packing whereas disordered structures result from high attraction potential in the suspension. Therefore, the structure depends on the particle size distribution and the developed attractive forces between the spheres. The change in surface charge of 310 nm and 100 nm spheres with pH is shown in Fig. 6. The isoelectric point (IEP) was determined to be about 3.4 for both sizes. The effect of the basic medium is reflected in the high zeta potential values where the surface charge is high enough for the suspension to remain stable, and may cause a long range ordering of spheres as shown in Fig. 5. Sacks and Tseng [24] reported that the zeta potential values for 500 nm silica spheres vary in the 5 to −70 range over the pH range of about 3–10. Higher absolute zeta potential values at pH 10 as shown in Fig. 6 may indicate that better state of dispersion can be achieved due to the presence of repulsive electrostatic forces between spheres.

Thermal and densification behaviour of 310 nm spheres are given in Fig. 7. The total weight loss of spheres was about 12% while the total dimensional shrinkage was 28% upon heat treatment at 1300 °C. Considerable weight loss was observed up to about 150 °C, which can be attributed to the removal of water and ethanol. Between 300 and 600 °C mostly removal of residual organic species and further polymerisation of the silica network along with the removal of surface OH^- groups may be responsible for the weight loss. There was almost no weight change in the ~700–1000 °C range. The small level of weight gain (~0.5%) above 1000 °C may probably be due to the oxidation of carbon rich inner surfaces in the bulk of the spheres during the relatively fast densification/crystallisation/coarsening of the microstructure in the 1000–1300 °C range. The developing structure finally is fully crystalline and in the cristobalite phase structure after heat treatment at 1300 °C as will be discussed later. As compared to acid catalysed systems consisting of linear, slightly cross linked polymeric species, base catalysed reactions lead to the formation of particulate structures which may have less entrapped organics. In a review paper by James [25], it was reported that a temperature of approximately about 1050 °C is required to densify the base catalysed systems while temperature of 700 °C is sufficient for polymeric gels. Brinker et al. [26] have identified three characteristic temperature ranges for multicomponent borosilicate gels. Range I (25–150 °C), weight loss with negligible shrinkage, range II (150–525 °C), considerable weight loss and shrinkage, and range III (525–700 °C) large shrinkage with small weight loss. These regions are also present for 310 nm

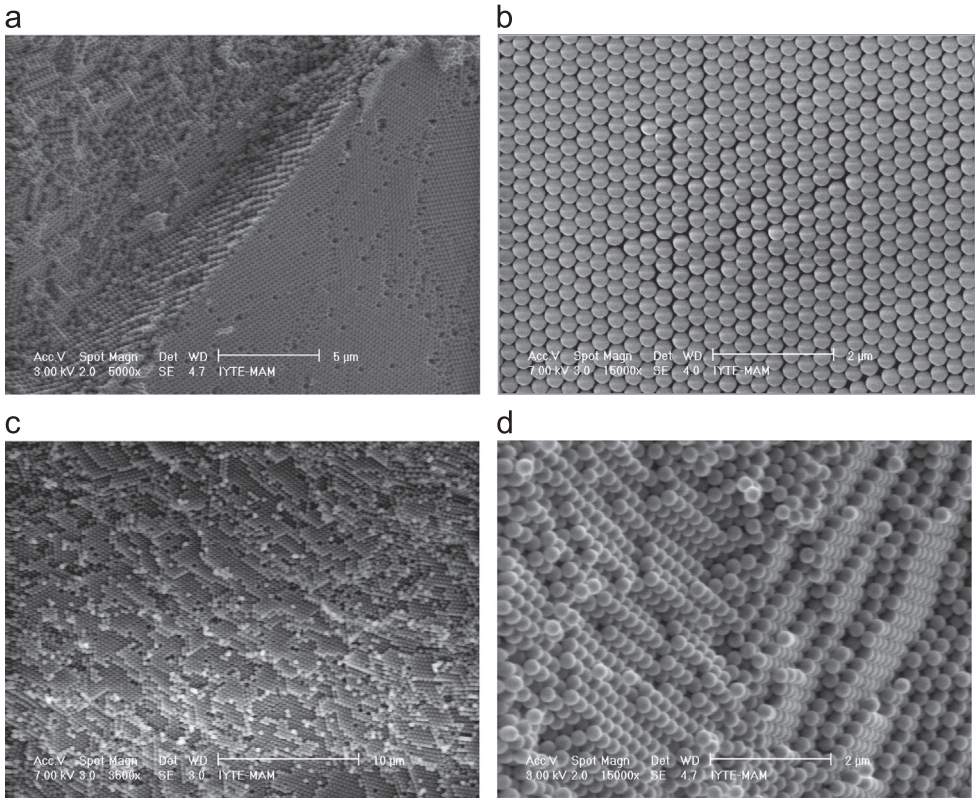

Fig. 5. SEM micrographs of 310 nm sphere (a) ordered compacts (5kX), (b) top surface (15kX), (c) fracture surface (3.5kX) and (d) fracture surface (15kX).

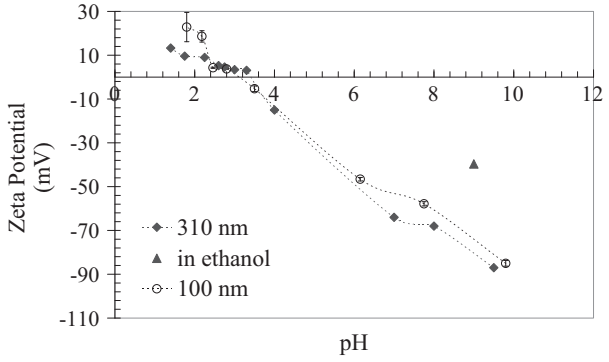

Fig. 6. The variation of zeta potential and pH ($^{\Delta}$: zeta potential in ethanol).

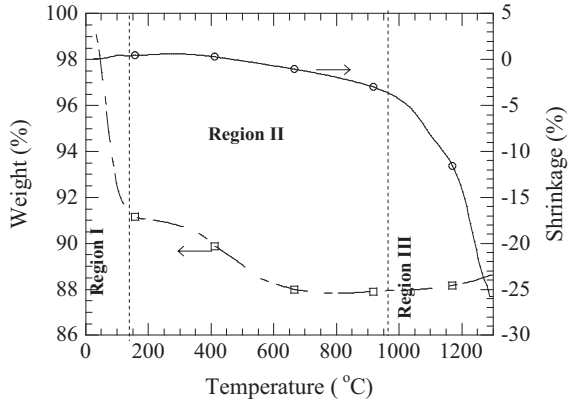

Fig. 7. TGA and shrinkage curves of 310 nm spheres.

silica spheres with corresponding shifts to higher temperature ranges indicating the stability of the microstructure as shown in Fig. 7. In region I where weight loss occurs due to desorption of physically bound water and alcohol, shrinkage predominantly was due to the increased capillary stresses caused by solvent removal. The removal of water formed through the polycondensation and the oxidation of organic residues can be responsible from the weight loss in region II. Shrinkage in this range resulted from skeletal densification which occurs by two mechanisms: by polycondensation reactions with formation of additional ≡Si–O–Si≡ linkages and loss of water, and by structural relaxation which occurs by atomic movements in the network without expulsion of water. Finally, in range III, rapid shrinkage occurs by viscous sintering in which tiny pores collapse, although hydroxyl condensation and structural relaxation also contributes to the observed shrinkage [25].

The OH^- groups exist primarily on the surfaces of silica particulate structures. This is consistent with the observation on the sintering behaviour of 310 nm spheres shown in Fig. 7. The increase in sphere size from 50 to 500 nm shifted the highest shrinkage rate temperature from ~1120 °C to 1240 °C as shown in Fig. 8. Higher temperature is required to densify particulate silica systems by viscous sintering [27]. The number of hydroxyl groups increases and their distribution becomes more uniform thus enhancing viscous flow sintering as the sphere size is reduced [25]. Brinker et al. [28] reported that microstructure has a significant effect on gel densification

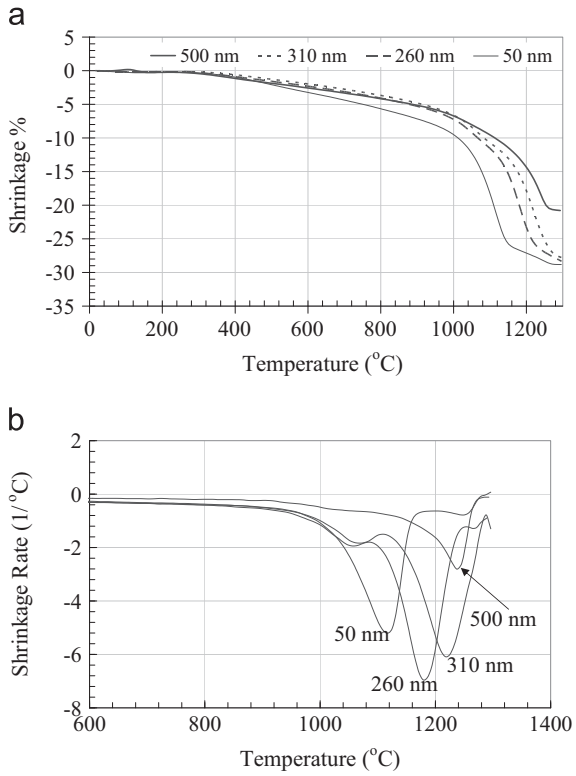

Fig. 8. Sphere size effect on (a) linear shrinkage, (b) shrinkage rate values.

and sintering models show an inverse dependence of shrinkage rate on sphere size or pore size.

The microstructural change of 50 and 310 nm spheres with heat treatment temperature in the 900–1200 °C range has been evaluated by using SEM micrographs given in Fig. 9. Although, at 900 °C, there is no evidence of sintering for 310 nm spheres, 50 nm spheres begin to become sinter active and at high temperatures greater regions are sintered that cause the collapse of the structures at 1100 °C. The onset of sintering for 310 nm on the otherhand is visible at 1100 °C.

XRD patterns of the 310 nm spheres sintered in the 900–1200 °C range are given in Fig. 10. The amorphous nature of the sphere compact has been conserved up to 1200 °C at which cristobalite crystals begin to nucleate and complete transformation to cristobalite was observed after heat treatment temperature to 1300 °C as shown in Fig. 11.

Sintering mechanisms in polycrystalline materials mainly are controlled by solid-state diffusion while the mechanism of sintering in amorphous materials is viscous flow [27]. The shrinkage rate of two monosize spheres as their centres approach can be calculated by using a theoretical model based on the Frenkel approach describing the early stage of sintering of spherical monodisperse particles. The energy gained by the decrease in surface area during densification is equal to the energy dissipated for viscous flow. Frenkel's model is valid within the first 10% of linear shrinkage in which there is considerable neck growth but insignificant densification [29,30]. Corrected neck growth between two spherical particles can be generalised to describe linear rate of shrinkage of an array of particles

$$\frac{L}{L_o} = 1 - \frac{3\gamma t}{8\eta R} \tag{6}$$

where L_o is the initial length, γ is the surface energy, (0.3 J/m^2), R is the particle radius, η is the viscosity and t is the time. Eq. (6) is valid if there is a linear relationship between (L/L_o) and time and the corresponding slope which can be used for the determination of the viscosity. Fig. 12 shows the linear relationship between dimensional changes over the sintering time of 45 min for 310 nm spheres sintered at different temperatures. The viscosities were determined as 1.53×10^{11} Pa·s, 1.2×10^{11} Pa·s, and 0.64×10^{11} Pa·s for 1000, 1050 and 1100 °C sintered samples, respectively.

Fig. 13 shows the predicted and measured values of dimensional changes of spheres heat treated at different temperatures. The solid lines in the figures show the predicted L/L_o values according to the Frenkel model. The predicted shrinkage approached more significantly to the experimentally determined shrinkages in the later stages of sintering for all samples. This model predicts the shrinkage rate by neglecting particle rearrangement during the densification. The non-uniformity in packing may be responsible from the significantly larger shrinkage values compared to the model predicted shrinkages. Another model that uses a simple geometrical approach is the Mackenzie and Shuttleworth (MS) approach. In this model, energy dissipation is related to the change in surface area, and the rate of densification of the viscous body containing closed spherical pores is elucidated in the final stages of densification [31]. This model provides a theoretical relation between the relative density and reduced times, $K(t-t_o)$, as shown in Fig. 14a where t_o is a fictitious time when the relative density is zero and K is given by Sacks and Tseng [29] as,

$$K = \frac{\gamma n^{1/3}}{\eta} \tag{7}$$

where n is the number of pores per unit volume and can be expressed by

$$n = \frac{P}{4\pi R^3/3} \tag{8}$$

where P is the number of pores per particle and it was estimated as 1 for uniform microstructure by assuming simple cubic packing [30]. Experimental values were fitted to the MS model by plotting reduced times derived from theoretical curve (Fig. 14a) versus sintering times corresponding to the experimentally measured densities as shown in Fig. 14b. The complete agreement between experimental values and theoretical curves was found for each temperature. On the other hand, non-linearity in Fig. 14b was eliminated by excluding the low temperature values for 1000 and 1050 °C heat treated samples. As stated in the study of Sacks and Tseng [29] increase in viscosity associated with the removal of residual OH^- groups in the initial period of heating causes the decrease in K values. The K value was calculated from the slope of the plots that allows the estimation of the viscosities at each temperature.

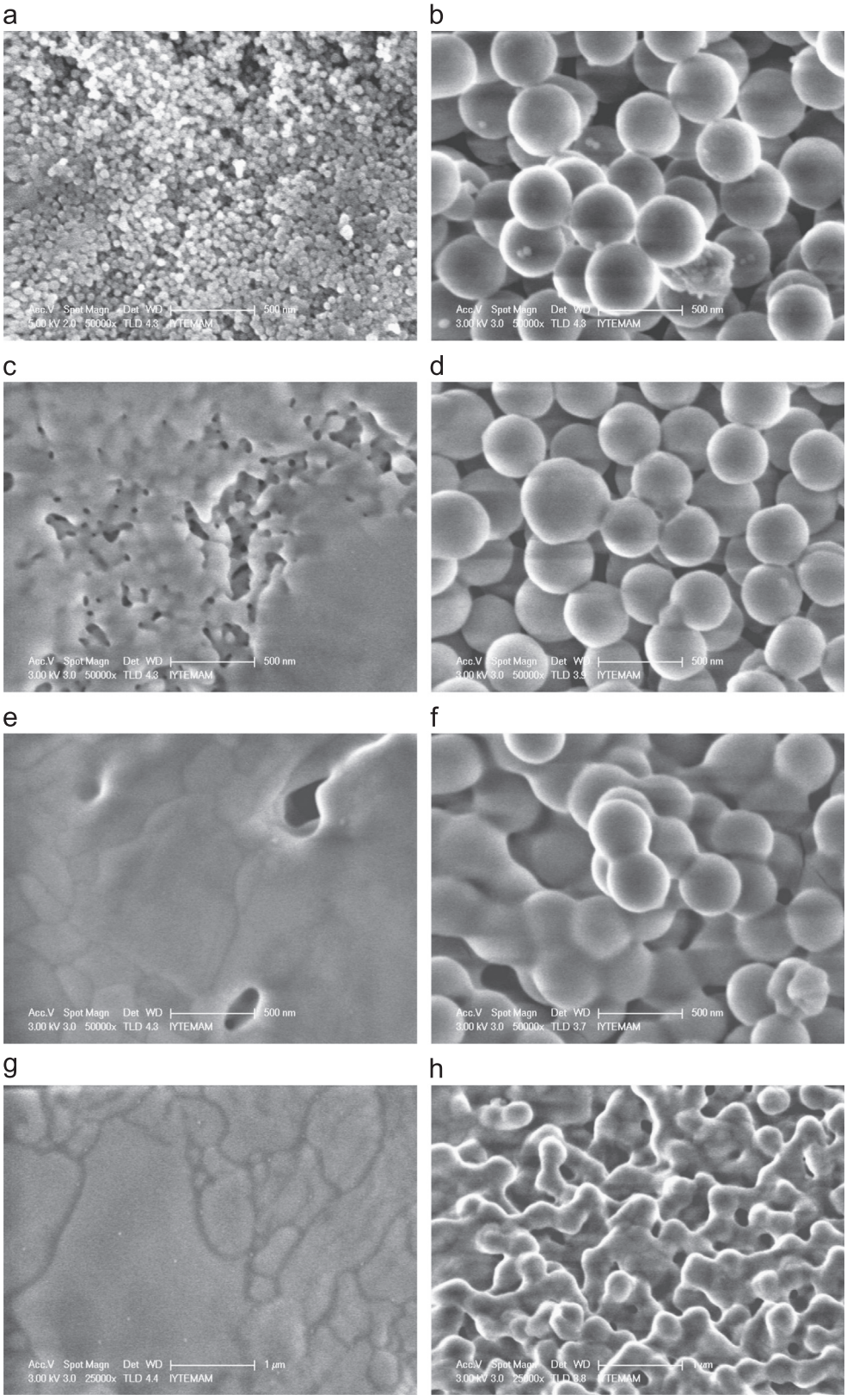

Fig. 9. SEM micrographs of 50 and 310 nm spheres heat treated at 900 °C (a-b), 1000 °C (c-d), 1100 °C (e-f) and 1200 °C (g-h). The holding time was 5 min.

The viscosities were determined as 15.2×10^{11} Pa·s, 8.34×10^{11} Pa·s, and 1.6×10^{11} Pa·s for 1000, 1050 and 1100 °C heat treated samples, respectively. These values are higher than those calculated from Frenkel's model. The assumption of constant viscosity in the course of initial stage of sintering might be ineffective for describing the densification

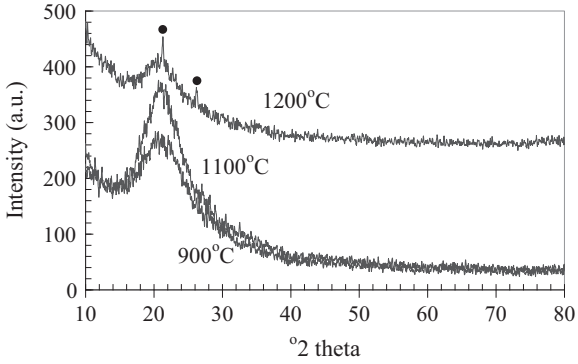

Fig. 10. XRD patterns of 310 nm sized spheres treated at different temperatures (●, cristobalite, JCPDS, file 76-0941).

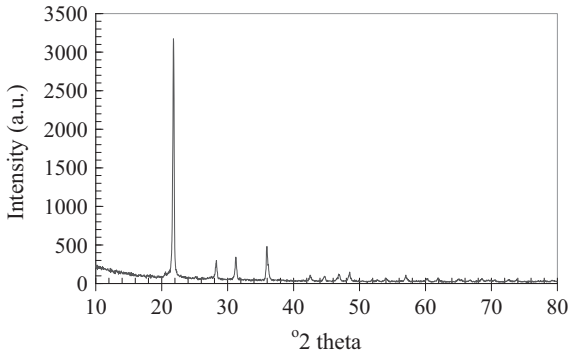

Fig. 11. XRD pattern of 310 nm sized sphere treated at 1300 °C (JCPDS, file 76-0941).

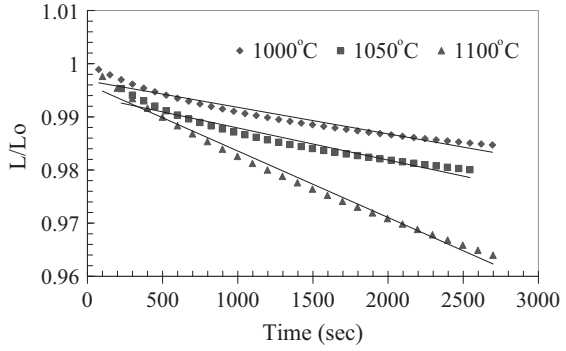

Fig. 12. Dimensional changes with time during the sintering of 310 nm spheres.

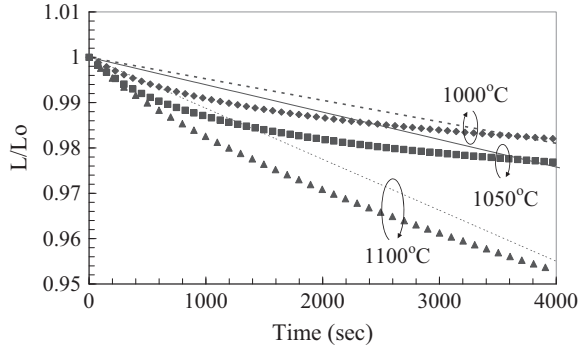

Fig. 13. Predicted and measured dimensional changes of samples sintered at different temperatures.

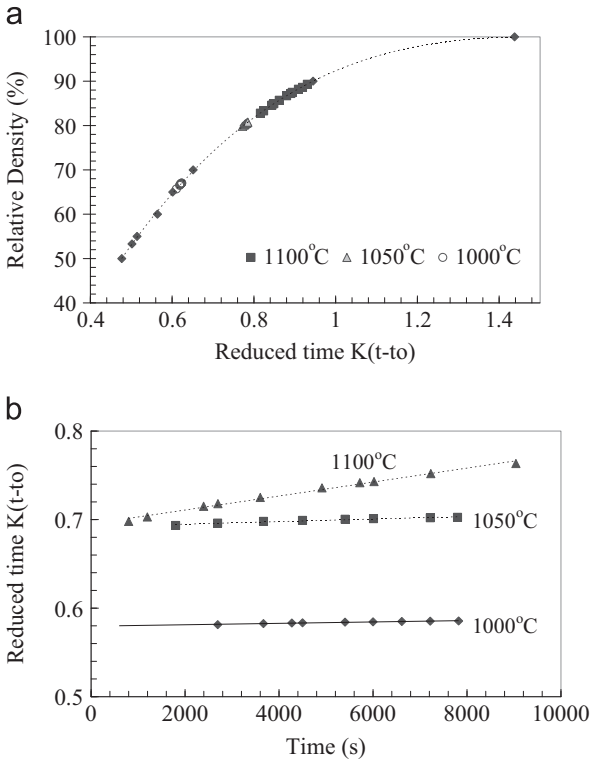

Fig. 14. Plot of reduced times (MS model) vs experimental sintering times for 310 nm spheres.

behaviour because of surface hydroxyl groups. Fig. 15 indicates the temperature–viscosity relationship with the varying OH^- contents. It can be observed that when silica contains more hydroxyl ions it becomes less viscous due to the creation of non-bridging bonds such as silanol (Si–OH) groups that replace siloxane (Si–O–Si) bonds [32]. The solid circles and squares represent the viscosities of 310 nm spheres determined from the Frenkel and MS models. Significantly lower viscosities compared to the reported values [27] might be due to higher contents of OH^- for the sol–gel derived 310 nm silica spheres.

The viscosity values of 310 nm spheres are plotted in Fig. 16 according to Arrhenius equation for both models

$$\eta = \eta_o \exp\left(\frac{Q}{RT}\right) \tag{9}$$

where Q is the activation energy and the η_o is pre-exponential constant. The calculated activation energies for the Frenkel and MS models are 125 kJ/mol and 335 kJ/mol, respectively. Although there is almost a linear relationship between shrinkage and time (Fig. 12) for the Frenkel model, the assumption of constant viscosity during initial stage of sintering may weaken the model results. The activation energy of 335 kJ/mol determined by using MS model which is based on the later stages of densification most probably is a more reliable value

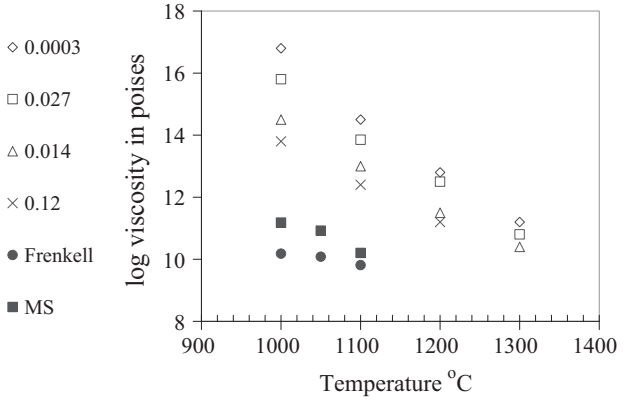

Fig. 15. The viscosity of silica as a function of sintering temperature with hydroxyl contents (wt%) [27].

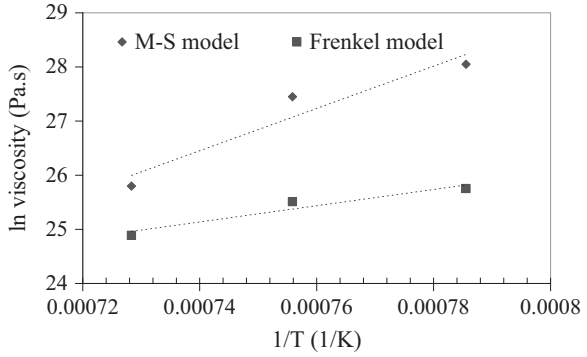

Fig. 16. Change in viscosity with sintering temperature calculated from the Frenkel and MS models (sphere size: 310 nm).

compared to that determined by using the Frenkel model. These activation energies are substantially lower than 506 and 494 kJ/mol determined by using MS and Scherer model, respectively for 500 nm spheres in another earlier work [28]. Brinker and Scherer [32] stated that activation energy decreases as the hydroxyl content increases. The calculated substantially low activation energy may probably be related to the presence of a significant level of silanol groups which was also shown to be probable because of the relatively lower viscosities determined in the present work.

4. Conclusions

Monodisperse silica spheres 50–520 nm in size were prepared by using the Stober process. Diffusive type of growth was determined by Nielsen chronomal analysis as a dominant growth mechanism for 520 and 310 nm monodisperse silica spheres. The densification behaviour of the spheres indicated an inverse dependence of shrinkage rate on the sphere size due to viscous sintering. The activation energies for viscous sintering according to the Frenkel and MS models were determined as 125 kJ/mol and 335 kJ/mol, respectively. The calculated substantially low activation energies might be related to the significant amount of silanol groups present in the amorphous structures during densification which was also shown to be probable through the determined relatively low viscosities.

References

[1] Y. Xia, B. Gates, Y. Yadong, Y. Lu, Monodispersed colloidal spheres: old materials with new applications, Adv. Mater. 12 (10) (2000) 693–713.
[2] Z.Z. Gu, A. Fujishima, O. Sato, Fabrication of high quality opal films with controllable thickness, Chem. Mater. 14 (2002) 760–765.
[3] S.H. Park, Y. Xia, Macroporous membranes with highly ordered and three-dimensionally interconnected spherical pores, Adv. Mater. 10 (13) (1998) 1045–1048.
[4] S. Wong, V. Kitaev, G.A. Ozin, Colloidal crystal films: advances in universality and perfection, J. Am. Chem. Soc. 125 (2003) 15589–15598.
[5] E. Matijeviç, Monodispersed metal (hydrous) oxides—a fascinating field of colloid science, Acc. Chem. Res. 14 (1981) 22–29.
[6] W. Stober, A. Fink, E. Bohn, Controlled growth of monodisperse silica spheres in the micron size range, J. Colloid Interface Sci. 26 (1968) 62–69.
[7] G.H. Bogush, M.A. Tracy, C.F. Zukoski, Preparation of monodisperse silica particles: control of size and mass fraction, J. Non-Cryst. Solids 104 (1988) 95–106.
[8] A. van Blaaderen, J.V. Geest, A. Vrij, Monodisperse colloidal silica spheres from tetraalkoxysilanes: particle formation and growth mechanism, J. Colloid Interface Sci. 154 (2) (1992) 481–501.
[9] D.L. Green, J.S. Lin, Y.-F. Lam, M.Z.-C. Hu, D.W. Schaefer, M.T. Harris, Size volume fraction, and nucleation of stober silica nanoparticles, J. Colloid Interface Sci. 266 (2003) 346–358.
[10] B. Topuz, Ph.D. dissertation, İzmir Institute of Technology, İzmir, Turkey, 2009.
[11] V.K. Lamer, R.H. Dinegar, Theory, production and mechanism of formation of monodispersed hydrosols, J. Am. Chem. Soc. 72 (11) (1950) 4847–4854.
[12] K. Lee, J.-L. Look, M.T. Harris, A.V. McCormick, Assessing extreme models of the stober synthesis using transients under a range of initial composition, J. Colloid Interface Sci. 194 (1997) 78–88.
[13] K. Nozawa, H. Gailhanou, L. Raison, P. Panizza, H. Ushiki, E. Sellier, J.P. Delville, M.H. Delville, Smart control of monodispersed stöber silica particles: effect of reactant addition rate on growth process, Langmuir 21 (2005) 1516–1523.
[14] H. Boukari, J.S. Lin, M.T. Harris, Probing the dynamics of the silica nanostructure formation and growth by SAXS, Chem. Mater. 9 (11) (1997) 2376–2384.
[15] H.N. Ch'ng, J. Pan, Sintering of particles of different sizes, Acta Mater. 55 (2007) 813–824.
[16] L. Ding, R.L. Davidchack, J. Pan, A molecular dynamics study of sintering between particles, Comput. Mater. Sci. 45 (2) (2009) 247–256.
[17] V. Tikare, M. Braginsky, Numerical simulation of solid-state sintering: I sintering of three particles, J. Am. Ceram. Soc. 86 (1) (2003) 49–53.
[18] D. Pontoni, T. Narayanan, A.R. Rennie, Time-resolved SAXS study on nucleation and growth of silica colloids, Langmuir 18 (2002) 56–59.
[19] G. Oskam, Z. Hu, L.R. Penn, N. Pesika, P.C. Searson, Coarsening of metal oxide nanoparticles, Phys. Rev. E 66 (2002) 011403-1–011403-4.
[20] J.H. Jean, T.A. Ring, Nucleation and growth of monosized TiO_2 powders from alcohol solution, Langmuir 2 (1986) 251–255.
[21] R.K. Iler, The Chemistry of Silica, Wiley, New York, 1979.
[22] D.J. Tobler, S. Shaw, L.G. Benning, Quantification of initial steps of nucleation and growth of silica nanoparticles: an in-situ SAXS and DLS study, Geochim. Cosmochim. Acta 73 (2009) 5377–5393.
[23] J.V. Sanders, Colour of precious opal, Nature 4 (1964) 1151–1153.
[24] M.D. Sacks, T.-Y. Tseng, Preparation of SiO_2 glass from podel powder compacts: I, formation and characterization of powders, suspensions, and green compacts, J. Am. Ceram. Soc. 67 (8) (1984) 526–532.
[25] P.J. James, The gel to glass transition: chemical and microstructural evolution, J. Non Cryst. Solids 100 (1988) 93–114.

[26] C.J. Brinker, G.W. Scherer, E.P. Roth, Sol–gel–glass: II, physical and structural evolution during constant heating rate experiments, J. Non-Cryst. Solids 72 (1985) 345–368.
[27] C.J. Brinker, G.W. Scherer, Sol–Gel Science: The Physics and Chemistry of Sol–Gel Processing, Academic Press, Boston, 1990.
[28] C.J. Brinker, K.D. Keefer, D.W. Schaefer, C.S. Ashley, Sol–gel transition in simple silicates, J. Non-Cryst. Solids 48 (1982) 47–64.
[29] M.D. Sacks, T.-Y. Tseng, Preparation of SiO_2 glass from model powder compacts: II, sintering, J. Am. Ceram. Soc. 67 (8) (1984) 532–537.
[30] G.W. Scherer, Sintering of sol–gel films, J. Sol–Gel Sci. Technol. 8 (1997) 353–363.
[31] G.W. Scherer, Viscous sintering of a bimodal pore-size distribution, J. Am. Ceram. Soc. 67 (11) (1984) 709–715.
[32] C.J. Brinker, G.W. Scherer, Sol–gel–glass: I, gelation and gel structure, J. Non-Cryst. Solids 70 (1985) 301–322.